Spectroscopic review of hydrogenated, carbonated and oxygenated group IV alloys

de Vrijer, Thierry; Bouazzata, Bilal ; Smets, Arno H.M.

DOI
10.1016/j.vibspec.2022.103387

Publication date
2022

Document Version
Final published version

Published in
Vibrational Spectroscopy

Vibrational Spectroscopy 121 (2022) 103387

Contents lists available at ScienceDirect

Vibrational Spectroscopy

journal homepage: www.elsevier.com/locate/vibspec

Spectroscopic review of hydrogenated, carbonated and oxygenated group IV alloys

Thierry de Vrijer [a,*], Bilal Bouazzata [a], Arno H.M. Smets [a]

[a] Photovoltaic Materials and Devices, TU Delft, Mekelweg 4, Delft 2628CD, the Netherlands

ARTICLE INFO

Keywords:
Infrared (IR) spectroscopy
Raman spectroscopy
Hydrogen bonding
Group IV alloys
Amorphous silicon and germanium
Electrical screening

ABSTRACT

Semiconductors based on group IV elements are widely used in the fields of micro-electronics, optics and photonics. The group IV alloys are processed using plasma enhanced chemical vapor deposition and its opto-electrical properties are a result of the material composition and structure. Infrared and Raman spectroscopy are complementary and powerful tools for providing these essential material characteristics. In this work, the vibrational modes present in hydrogenated, oxygenated and carbonated group IV alloys are investigated in a unique range of amorphous and nano-crystalline $Si_{X\geq 0}Ge_{1-X}$:H films and their alloys with C, O and Sn. Measurements are performed both post-deposition and following extended exposure to the ambient and de-ionized water. This comprehensive review is of value in the fields of material science and engineering as a single work of reference for group IV peak identification. Additionally, the effect of electrical screening, the influence of the dielectric medium on the peak frequency of a vibrational mode, is illustrated using the experimentally observed frequency shifts of X-O and X-H (X = C, Si, Ge) vibrational modes. All experimentally observed center frequencies of silicon hydride stretching modes in silicon solids and corresponding silicon-hydride configurations are identified using a straightforward Lorentz-Lorenz model approximation and considering all potential hydrogenated volume deficiencies within a tetrahedrally coordinated amorphous and nanocrystalline lattice. It shows that the stretching mode signature can reveal detailed information on the volume deficiencies in IV-valence alloys.

1. Introduction

Semiconductors based on group IV elements like silicon, carbon, and germanium are widely used in the fields of micro-electronics, optics and photonics, for a range of applications including transistors, detectors, displays and photovoltaics. The performance of devices in which group IV semiconductors are applied, is a result of the opto-electrical properties and chemical stability of group IV alloys, which in turn are a direct result of the chemical composition and structural characteristics of the material. Understanding of these material properties is therefore crucial for optimization of hydrogenated group IV alloys. Vibrational spectroscopy has proven an important means of providing essential information related to the material stoichiometry [1–4], concentration of elements like hydrogen [5–9], the void fraction and porosity [10–14], the preferential bonding of elements in stoichiometric films [15–17], the chemical stability of films [18,20,26] and the amorphous and crystalline material phase fractions [19,21–23]. While Fourier-transform infrared spectroscopy (FTIR) and Raman Spectroscopy (Raman) are often used tools in material characterization, works combining results of these complementary techniques for group IV alloys are scarce, as are works presenting more than a single alloy of varying stoichiometry. Such a comprehensive review of group IV alloys is of great value as a reference for peak identification. Additionally, trends across the center frequencies of vibrational groups in group IV alloys, as a function of the period and group of an element, can provide insight for the identification of peaks during the development of novel alloys.

For that reason, in this work, a range of group IV amorphous (a-) and nano-crystalline (nc-), unalloyed and alloyed, hydrogenated (:H) materials are processed of varying elemental composition. A nano-crystalline material is a heterogeneous material in which nanometer-scale crystals are embedded in an amorphous phase. FTIR and Raman spectroscopy measurements and energy dispersive X-Ray (EDX) compositional analysis are performed on these plasma enhanced chemical vapor deposition (PECVD) processed undoped films. Vibrational spectroscopy is based on measuring the vibrational modes of single or group of chemical bonds in molecules up to solids. FTIR and Raman analysis are complementary vibrational techniques. In infrared absorption the absorbed photon matches the energy differences between the vibrational energy states.

* Corresponding author.

https://doi.org/10.1016/j.vibspec.2022.103387
Received 1 March 2022; Received in revised form 21 April 2022; Accepted 21 May 2022
Available online 7 June 2022

FTIR detects bonded atoms with a strong dipole moment that undergo a photo-induced change in dipole moment. Raman spectroscopy is based on the inelastic scattering of photons in which the shifts of the photon energy reflects the energy difference between the vibrational modes. Raman detects bonded atoms with a weak dipole moment that exhibit a photo-induced change in polarization. Here, these measurements are performed before and after the films are subjected to different degradation conditions in the dark and under light, in the ambient and in de-ionized (DI) water. This extensive experimental design provides the opportunity to compare vibrational spectra in 3 unique ways: 1. a comparison between homogeneous and heterogeneous materials with different material phases, 2. a comparison of the presence and peak frequency of oxide and hydride vibrational modes across the group IV elements carbon, silicon and germanium and 3. a comparison of the vibrational spectra between the state immediately after deposition and following exposure to different ambient and illumination conditions.

The purpose of this work is twofold. For one, the added value of this unique experimental design, for the fields of material science and engineering, is in providing a comprehensive overview of the vibrational spectra of group IV alloys. In addition to providing a single work of reference for peak identification, a fundamental perspective is presented on the peak frequencies as a function of the material structure and elemental composition. Moreover, throughout this work examples are provided of the applications of vibrational spectroscopy for relating material characteristics to opto-electrical properties, chemical stability and/or device performance. The discussion section of this work consists of four main parts. In the first part of the discussion, Section 3, the as-deposited FTIR spectra of the a/nc-$Si_{X\geq 0}Ge_{1-X}$:H films and their alloys with C, O and Sn are characterized. The peak frequencies of the hydrides, and potential applications of hydride identification, are described in Section 3.1, and the oxides and carbides in Section 3.2, respectively. Following these descriptive sections, a reflection on the relation between subtle shifts of FTIR vibrational frequencies and the physical and chemical nature of the local environment of vibrational excited chemical bonds in a solid is presented in Section 4. In Section 5, the Raman spectra are analyzed, with a focus on the amorphous and crystalline (c-) peaks in Section 5.1, followed by the hydride-, oxide- and carbide-bonds in Section 5.2. Finally, in Section 6, a reflection is presented on the potential subjective nature of the peak fitting process in heterogeneous, chemically complex group IV alloys.

2. Experimental section

2.1. Film processing

The films presented in this work are processed on 4 in., 500 μm thick monocrystalline silicon wafers. The a/nc-Ge:H and a-GeCSn:H films were processed in the Cascade radio-frequency (RF) PECVD reactor, which has a circular electrode with a diameter of 160 mm and an electrode spacing of 20 mm. Cascade is a laminar flow reactor, where germane (GeH_4) and molecular hydrogen are used as precursor gasses. Additionally, for the GeCSn:H depositions, tetramethyltin (TMT) (Sn $(CH_3)_4$) is used as a precursor. Injection of TMT into the reactor is controlled through a valve, for which the open and close time can be controlled. The ratio of the close time to the open time is referred to as the duty cycle in table 1. More information can be found in [24]. All other films were processed in a different RF-PECVD cluster tool. In this cluster tool the intrinsic (i-) a-Si:H, i-nc-Si:H and remaining films (i-a/nc-SiGe:H, a-GeO:H, nc-SiO:H, a-GeC:H, nc-SiC:H) films are processed in separate dedicated chambers, each with a flat 12 cm × 12 cm shower-head electrode. The deposition conditions of the processed films, including deposition times and thickness, are reported in Table 1. After deposition the wafers were cut in quarter pieces to measure the evolution of the vibrational spectra and opto-electrical parameters over time, as a function of degradation condition. Of each processed film, three quarters were stored in a temperature controlled room. One quarter was stored in the dark under ambient conditions. A second quarter was stored in an in-house light soaking setup, under ambient conditions. A third quarter was stored in the dark in a container filled with DI water. The vibrational and electrical parameters of these films were then measured at approximately 10 h, 100 h and 1000 h after deposition, with an additional measurement performed at 1hr after deposition for the samples stored in water.

2.2. Vibrational and elemental analysis

FTIR spectra were obtained using a Thermo Fisher Nicolet 5700 spectrometer. The Raman spectra were obtained using an inVia confocal Raman microscope with a laser operating at a wavelength of 514 nm. The EDX analysis was performed on a FEI Nova NanoSEM 450, using an acceleration voltage of 3 kV. The elemental composition was obtained by comparing the area of fitted gaussian distributions after background subtraction. As such, the elemental fractions represent atomic fractions rather than weight fractions. For the GeCSn:H sample an acceleration voltage of 5 kV was used, to include the main Sn electron transmission at around 3.44 keV in addition to the one at 0.69 keV. While this peak is not included in Fig. 1 for visualization purposes, it is included for determining the atomic fraction.

2.3. Fitting vibrational spectra

The spectra were fitted using the Fityk freeware [25]. The background was subtracted manually. Gaussian distributions were added manually. For each sample, the minimum number of Gaussians are used to accurately match the shape of the measured data. The process of determining the number of Gaussians is based on the experience of fitting and re-fitting the hundreds of intrinsic group IV alloys, presented in [21,24,26–29]. Following the manual fit, an autofit option was used to minimize the error between the measured data and the sum of the Gaussian distributions by determining the exact peak frequency, width

Table 1
Deposition conditions of the films presented in this work. Precursor gas flow rates indicated in standard cubic centimeters (sccm).

	P_{RF} (mW cm^{-2})	p (mbar)	T_S (°C)	SiH_4 (sccm)	GeH_4 (sccm)	CH_4 (sccm)	Sn $(CH_3)_4$ (duty cycle)	H_2 (sccm)	CO_2 (sccm)	Dep. time (s)	Thickness (nm)
a-Si:H	19.4	0.7	180	40						1100	177
nc-Si:H[a]	277.8	4	180	3.3				120		900	45.9
a-SiGe:H	20.8	3.6	180	30	5.3			200		2800	292.2
nc-SiGe:H	20.8	3.6	180	30	0.4			200		1100	148.1
nc-Ge:H	99.5	3.5	200		0.5			200		1680	222.6
a-Ge:H	24.9	4	200		0.5			200		2100	182.6
a-GeO:H	20.8	3.6	180		2			200	20	850	173.8
a-GeC:H	20.8	3.6	180		2	15		200		800	170.6
nc-SiC:H	20.8	3.6	180	5		10		200		1848	213.4
nc-SiO:H	20.8	3.6	180	5				200	5	1861	164.9
a-GeCSn:H	14.9	4	230		1.5		2857	200		570	91.0

[a] Processed at 40 MHz.

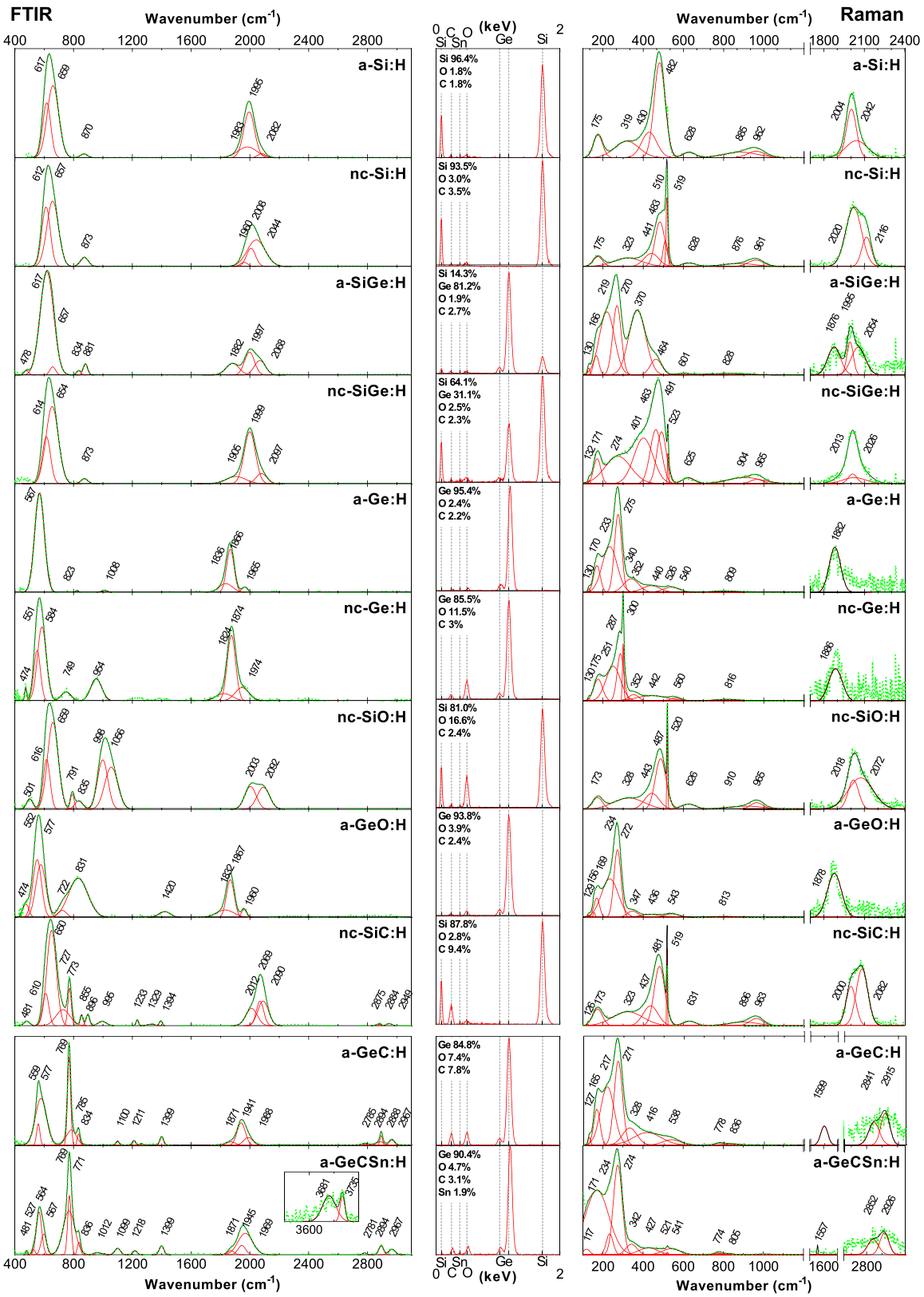

Fig. 1. Vibrational spectra of group IV elements. FTIR spectra (left) and Raman spectra (right) plotted as a function of wavenumber, for a/nc-$Si_{x\geq 0}Ge_{1-x}$:H and their alloys with C, O and Sn. The green dotted lines indicate the measured data after background subtraction. Gaussian distributions (red curves) are fitted to the experimental data. The black curves indicate the sum of the fitted Gaussians. The wavenumber of the peak frequencies of the fitted Gaussian curves are indicated in the figures. The atomic fractions of the presented materials are indicated in the center, as obtained by EDX analysis. Inset (bottom left) shows the 3500–3800 cm^{-1} range of the a-GeCSn:H sample. Note that the horizontal axis of the bottom two Raman plots (a-GeC:H and a-GeCSn:H) deviates from the plots positioned above.

and height of the Gaussian distributions. For bonding configurations with multiple hydrides, or other atoms or groups, the convention -X_n is used in this work. A reflection on the fitting process is presented in Section 6.

3. FTIR spectra of hydrogenated a/nc-$Si_{X\geq 0}Ge_{1-X}$:H and their alloys with Sn, C and O

The vibrational spectra and elemental analysis of a number of amorphous and nano-crystalline group IV materials and their alloys with carbon and oxygen are shown in Fig. 1. The measured curves are indicated in green, while the Gaussian distributions fitted to reproduce the curves are indicated in red. The sum of the fitted Gaussians is represented by the black curve. The peak frequencies of the fitted Gaussians are indicated in the spectra and an overview of the observed peaks is presented in Table 2, including the most likely origin of the vibrational modes. It should be noted that C and O fractions in the Ge(C,O):H and Si(C,O):H alloys are intentionally added during deposition using CO_2 and CH_4 precursor gasses, while C and O fractions in the a/nc-$Si_{X\geq 0}Ge_{1-X}$:H films are the results of post-deposition oxidation and carbisation reactions.

3.1. C,Si,Ge-hydrides

The hydrogen vibrational modes are often used as a tool for determining the hydrogen concentration in thin films, a relevant metric for relating structural characteristics to electrical material properties such as the bandgap energy and degree of electrical passivisation [65]. Moreover the specific configuration of the hydrogen stretching modes (SM) have proven an important tool for thin film analyses. The ratio between the low SM (LSM) and high SM (HSM), visualized for Si-H stretching in Fig. 4, are used as a metric for determining void fraction and material density in thin a-Si:H [10–12,14], a-SiGe:H [13] and a-Ge:H [21,27] films. Moreover, in nc-Si:H, the specific SM signature is used to optimize the growth of device quality films photovoltaic applications [52].

None of the a/nc-Si:H and a/nc-SiGe:H (a/nc-$SiGe_{X\geq 0}$:H) show significant traces of oxygen or carbon contamination according to EDX, which aids in the identification of hydride vibrational modes in these samples. The a/nc-$SiGe_{X\geq 0}$:H spectra appear quite similar, which is not unexpected, since Si—Ge bonds are not FTIR active and hydrogen is reported to favorable bond with silicon in PECVD processed a-SiGe:H alloys [17,66,67]. The peaks in the a/nc-$SiGe_{X\geq 0}$:H FTIR spectra are therefore expected to be silicon hydrides with a small fraction of germanium hydrides in the SiGe:H samples. In the four a/nc-$SiGe_{X\geq 0}$:H samples two peaks are observed in the 500–800 cm^{-1} range which are related to Si-H wagging modes [9,20,35,37]. The peak observed at around 870–881 cm^{-1} is likely related to Si-H_n bending [9,20,35,36,52]. In the nc-SiC:H films, Si-H_n bending is slightly shifted to higher wavenumbers, likely due to the presence of carbon in the local environment. The four a/nc-$SiGe_{X\geq 0}$:H samples all exhibit several peaks in the 1850–2200 cm^{-1} range, which are related to Si-H_n stretching modes [20,52,64]. A detailed description of the exact identification and frequency of the different Si-H SM's in this range is presented in Section 4. There seems to be no significant Si-H_3 SM, which would reportedly result in a vibrational mode at 2140 cm^{-1} [52,68]. In the a/nc-$SiGe_{X\geq 0}$:H samples an additional peak appears, located at around 1875 cm^{-1}, that coincides with peaks in the a-Ge:H and nc-Ge:H spectra. This peak is related to Ge-H_n SM's [7,13,26,32,33,35,36,63]. The a/nc-Ge:H FTIR spectra look very similar to the a/nc-Si:H spectra, except that the all peak frequency are shifted to lower wavenumbers. Ge-H_n wagging occurs at around 560–580 cm^{-1} [9,13,26,32–36], and Ge-H_n bending at about 750–760 cm^{-1} [13,32,36,47] and the Ge-H SM at 1875 cm^{-1} is accompanied by a Ge-H_n SM at approximately 1970 cm^{-1} [7,13,32,33,36,63].

Additionally, we consider the carbon hydrides, which can be found in the SiC:H and GeC(Sn):H spectra. Carbon hydride SMs appear in the 2800–3000 cm^{-1} wavenumber region [3,9,40–43,49,63]. C-H_n SMs manifest as three distinct peaks, with peak frequencies at around 2790 cm^{-1}, 2890 cm^{-1} and 2970 cm^{-1}. These peaks can also be observed in the GeC:H spectra in Fig. 2, where they are seen to increase with increasing CH_4 flow rate during deposition. In tandem with the C-H_n stretching, C-H_n rocking vibrations at 770 cm^{-1} and 830 cm^{-1} increase with CH_4 flow rate. Moreover, vibrations appear in the nc-SiC:H

Table 2
List of FTIR peaks identified in samples processed in this work. Vibration types, rocking (*Ro*), wagging (*W*), bending (*Be*), stretching (*St*), indicated in table.

Peak frequency (cm^{-1})	Suspected bond	Vibration	Refs.
480	C—O_x	*W*	[30,31]
560–580	Ge—H_n	*W*	[9,13,26,32–36]
610–660	Si—H_n	*W*	[9,20,35,37]
630	Ge—C_x	*St*	
650–950[a]	Ge—O_x	*St*	[1,9,26,32,38]
720–790	Si—C_x	*St*	[3,9,39–46]
750–760	Ge—H_n	*Be*	[13,32,36,47]
770	C—H_n	*Ro*	[48–51]
830	C—H_n	*Ro*	[49,50]
870–890	Si—H_n	*Be*	[9,20,35,36,52]
900–1200[a]	Si—O_x	*St*	[13,20,37,52,53]
990–1020	C—H_n	*W*	[3,37,40–44,46,51]
1100	C—O_x	*St*	[30,54,55]
1210–1230	C—H_n	*W*	[40,46,54]
1400	C—H_n	*Be*	[30,40,55–57]
1430–1450	(O_x)C—H_n	*Be*	[30,55,58,59]
1660	C═O_x	*St*	[54,59,60]
1740	H_nC—O_x	*St*	[61,62]
1800–2050	Ge—H_n	*St*	[7,13,32,33,35,36,63]
1850–2200	Si—H_n	*St*	[19,20,52,64]
2800–3000	C—H_n	*St*	[3,3,9,9,40,40,41,41,42,42,43,43,49,49,51,63]
3500–3800	O—H_n	*St*	[54]

[a] Manifests as a broad peak, that is the results of the superimposition of a range of X-O(H) vibrations, with the exact center peak frequency depending on the ratio of the bonds.

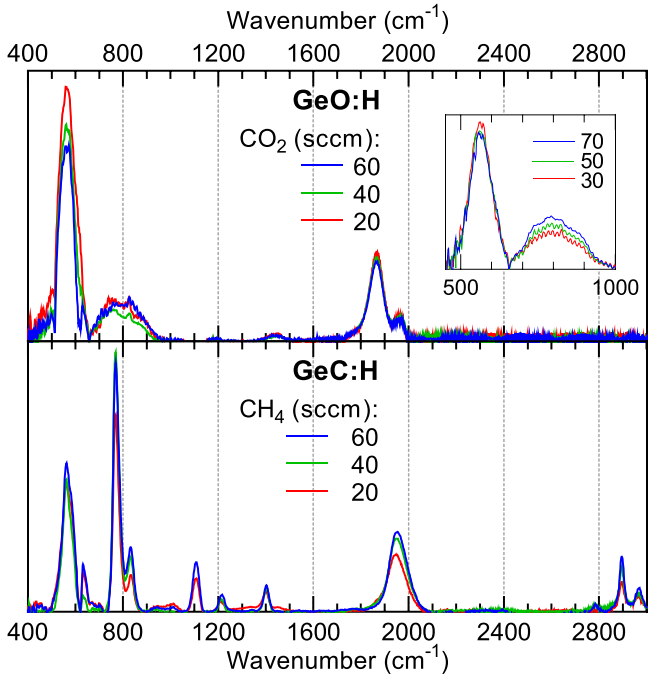

Fig. 2. FTIR spectra of a-GeO (top) and a-GeC samples (bottom) process at different CH_4 and CO_2 precursor gas flow rates. In the inset a second set of a-GeO samples is presented, processed at varying CO_2 flow rates.

spectrum in Fig. 1 and the GeC:H spectrum in Fig. 2 that are most likely the results of C-H_n wagging, in the 1020 cm^{-1} [3,37,40–44,46,51] and 1210–1230 range [40,46,54] and C-H_n bending at 1400–1450 cm^{-1} range [13,30,40,55–59].

Finally, O-H_n SMs can be observed in the inset in the GeCSn:H FTIR spectrum in Fig. 1. The O-H_n SMs appear up-shifted with respect to the group IV hydride SMs, approximately to the 3600–3800 cm^{-1} range [54]. Oxygen incorporation in the porous GeCSn:H film is the results of a post-deposition oxidation that occurs during the 1–2 min ambient exposure during the transfer from the PECVD reactor to the FTIR measurement setup. Interestingly, O-H_n incorporation is only observed in Ge-based alloys, whereas in porous Si-based alloys post-deposition oxidation only occurs due by oxygen incorporation in the Si—Si back bond resulting in Si—O—Si [27].

3.2. Si,Ge-oxides and carbides

The appearance of O-H_n SMs are a demonstration of the porous nature of a film, in which oxidation occurs readily. The monitoring of oxidation behavior is relevant for optimization towards a chemically stable, device quality material. Examples of FTIR analyses of the oxidation behavior of thin films include nc-Si:H [20,52], nc-SiGe:H [69] and a/nc-Ge:H [21,26,27]. In these works, the FTIR measurements do not only provide information on degree of oxidation and/or carbisation. Monitoring of the vibrational modes over time provides information on the type of chemical reaction that takes place and the local environment in which the degradation reaction occurs. Moreover, for samples in which O or C are intentionally added, vibrational spectroscopy can provide information on the material stoichiometry.

Considering the identification of oxide and carbide bonds in the group IV alloys presented in Fig. 1. Silicon-oxygen vibrations can be observed in the nc-SiO:H films, and to a lesser extent in the nc-SiC:H film, as a wide peak in the 900–1200 cm^{-1} range [20,37,52,53]. The peaks can be best approximated by two Gaussian distribution with center peak frequencies at around 990–1000 cm^{-1} and 1050 cm^{-1}. The exact type of Si-O vibrations is unclear, which is indicated in this work by the subscript "x". With respect to the Si-O_x vibrations, the Ge-O_x vibrations are down-shifted to about 650–1000 cm^{-1}, which is in line with our earlier work [21,26,27] and that of others [9,32,38]. Reports identify various Ge-O related vibrational modes in this range, such as the Ge-O-H mode with a peak frequency of 670 cm^{-1} [1], Ge-O-Ge at 750 cm^{-1} [1,9,13,15,32,38] and at 860 cm^{-1} [13,15]. Some Ge-O_x vibration is also likely the origin of the peak in the nc-Ge:H spectrum at 954 cm^{-1}.

It should be noted, considering the small carbon fraction in the a-GeO:H samples, that the presence of Ge-C related vibrations in the 650–1000 cm^{-1} range cannot be excluded. To facilitate identification of the Ge-O_x and Ge-C_x peaks, a number of GeO:H and GeC:H samples were processed, as shown in Fig. 2. For these samples, the CO_2 and CH_4 gas flow rates during deposition, the precursor gasses for oxygen and carbon integration, were varied. A few things can be observed from these spectra. First, with increasing CO_2 flow rate, the band of vibrations in the 650–1000 cm^{-1} range show an overall increase with respect to the Ge-H_n wagging vibrations. These peaks then are likely related to Ge-O_x vibrations. The distinct peaks at 770 cm^{-1} and 830 cm^{-1} are confidently assigned to C-H_n wagging vibrations, in line with earlier reports [3,9,40–46]. Similarly, the peak at approximately 1000 cm^{-1} is confidently assigned to C-H_n bending vibrations, in line with [3,37,40–44,46,51]. Both assignments are made considering the peak frequency in reference to Ge-H and Si-H wagging vibrations, the increase of peak intensity with CH_4 flow rate and the fact that these peaks appear in both the SiC:H and GeC:H FTIR spectra. It should be noted however that a number of different vibrations have been reported in this wavenumber range. At 770 cm^{-1} Ge-H vibrations have been reported [13,32,36,47], as well as Ge-O_x vibrations [1,13]. Similarly, the peak at 830 cm^{-1} has been attributed to Ge-O_x [32,38,70,71] and Ge-H vibrations [13,36,47,51]. Similarly, for the peak at around 1000 cm^{-1} Ge-C-C vibrations are reported [49,50], as well as C-O vibrations [72,73]. In section 6 we reflect on the multitude of peaks identified int his range.

Additionally, a small distinct peak appears at 620 cm^{-1} for higher CO_2 flow rates. This peak is matched by a stronger peak in the GeC:H spectra, and is therefore likely related to a Ge-C_x vibration, which reportedly occurs in this range [45,51,57,70,74,75]. A similar vibration, Si-C_x stretching, can be observed in the nc-SiC:H spectrum, where a peak is positioned in between those of the Si-H_n and C-H_n wagging vibrations. The exact peak frequency is a function of the local environment and assumptions during the fitting procedure, and consequently ranges from about 710–760 cm^{-1} in earlier reports [3,9,39–46].

Besides the Ge-H and C-H vibrations, two more peaks are present in the GeC:H spectra in Fig. 2. These peaks occur at 480 cm^{-1} and 1100 cm^{-1}. Considering that i) matching peaks, though small, can be observed in the GeO:H and nc-SiC:H spectra and ii) the frequency of the peaks in reference to the Ge-O_x and Si-O_x SMs, the latter is likely the result of C-O_x stretching [30,54,55] while the former is the result of C-O_x wagging [30,31].

3.3. FTIR-spectra after degradation

To better understand the vibrational modes in the group IV alloys presented in this work, the samples were stored under different conditions and the vibrational spectra were monitored over time. The FTIR and Raman spectra measured after a 1000 h of storage, unless indicated otherwise in the plots, are presented in Fig. 3.

A strong effect can be observed in the a/nc-Ge:H and a-GeO:H vibrational spectra. For the samples stored in water, the various Ge-H vibrational modes decrease over time. At the same time, the amorphous germanium Raman modes (100–300 cm^{-1}) disappear as well, exclusively leaving a c-Si peak at 520 cm^{-1} and a peak related to Si-O vibrations in the 900–1050 cm^{-1} range. This means that at this point the c-Si wafer and oxidized wafer surface are being measured, which indicates that Ge:H reacts strongly with the DI water, a reaction in which the Ge:H tissue is consumed. Note that these Raman modes will be discussed in more detail in Section 5. The consumption of the Ge:H film was confirmed by spectroscopic ellipsometry measurements, where a decreased film thickness was observed as a function of time.

During this consumption of Ge:H, additional vibrational modes appear over time that assist in the identification of peaks in the FTIR fingerprint region ($\omega \lesssim 1500$ cm^{-1}). These modes are the result of different bonding configurations between carbon, hydrogen and oxygen. In the a-GeO:H, a/nc-Ge:H and a/nc-SiGe:H spectra peaks appear at 1660 cm^{-1}, related to the C═O [54,60] or C-O vibration [59], and at 1740 cm^{-1}, related to either an H_3CO [61] or H_2CO [62] vibration. Additionally, in the a/nc-Ge(O):H spectra vibrational modes appear at around 1440 cm^{-1}, also present in the GeO:H spectra of Fig. 2, related to (O_x)C-H_n bending [30,55,58,59]. This post-deposition process during which carbon is integrated in the germanium alloys is discussed in detail elsewhere [27].

Finally, it is noteworthy that the monitoring of the vibrational modes in the a/nc-Ge(O,C):H films provides information on the resilience against water induced degradation. The resilience against oxidation is increased in the a-GeC:H samples, where CH_4 is added during deposition. Not only is the rate of film consumption decreased, the inherent stability of the GeC_x phase can also be observed in the 650–1000 cm^{-1} range in the a-Ge(O):H spectra. For the samples stored in water, unlike the samples stored in the ambient, the dominant vibration shifts over time, towards a peak frequency of 770 cm^{-1}, which is associated to Ge-C_x vibrations.

4. Physical relation between local environment and peak frequencies

The identification of the observed vibrational modes across the

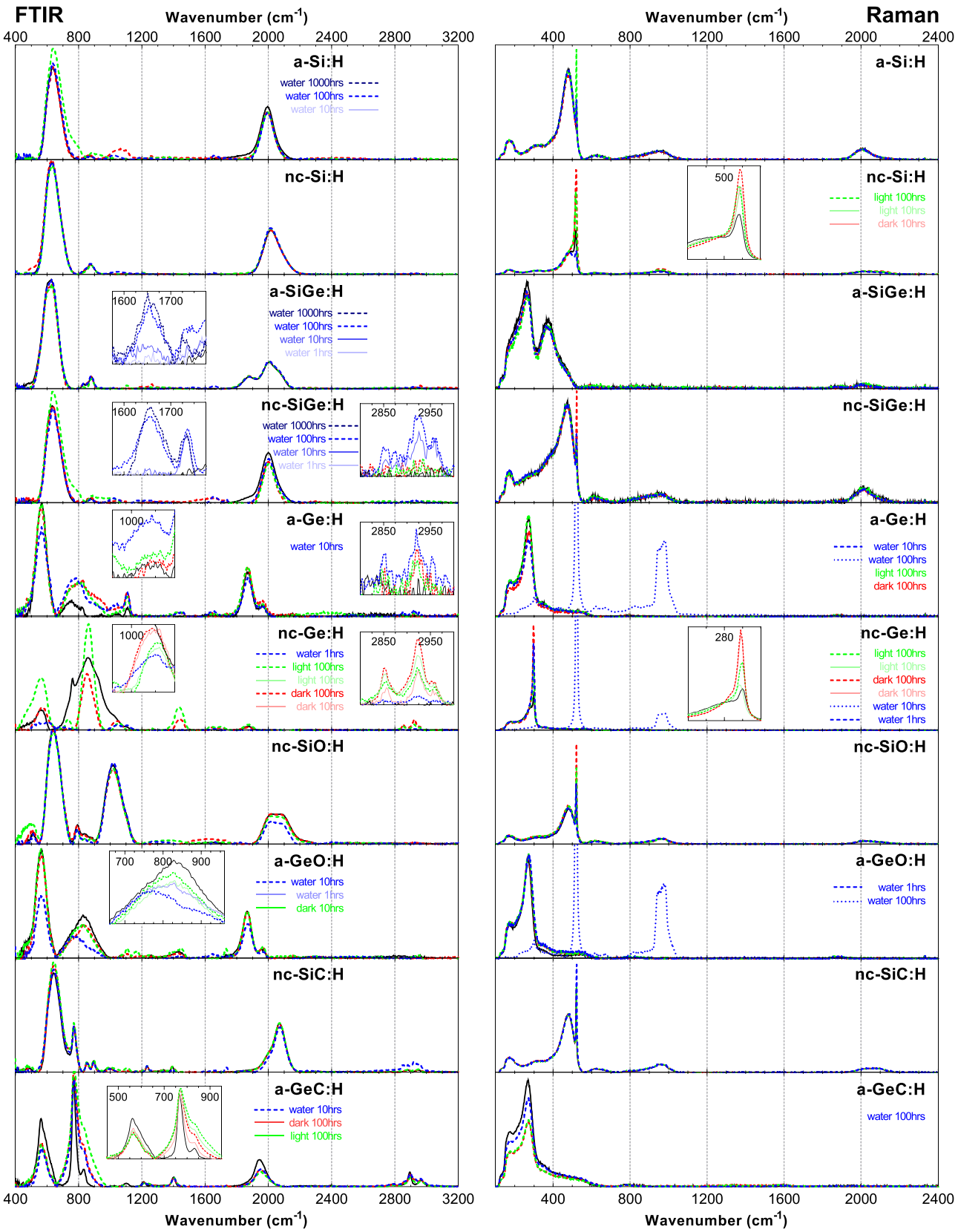

Fig. 3. Vibrational spectra of group IV elements. FTIR spectra (left) and Raman spectra (right) plotted as a function of wavenumber, for a/nc-$Si_{x\geq 0}Ge_{1-x}$ and their alloys with C, O and Sn. All curves are presented after background subtraction. The black solid curves represent measurements at 0 h. The dashed green curves indicate measurements after degradation in the light under ambient conditions. The dashed red curves indicate measurements after degradation in the dark under ambient conditions. The dashed blue curves indicate measurements after degradation in the dark in de-ionized water. The number of hours after degradation is indicated in the plots. Note that the insets are zoom-ins; the same data presented on a decreased vertical axis range for a selected wavenumber range.

different group IV alloys allows for a reflection on the physical relation between the peak position and local environment. The vibrating valence bonds like C-H_n, Ge-H_n, and Si-H_n are physically described as dipole vibrations. The effective charge of a vibrating mono-hydride X-H (X = C, Si, Ge, Sn) is determined by valence electrons that make the valence Si—H bond, whereas the effective mass of the vibrating system is mainly determined by the mass of the hydrogen atom, assuming that the position of the X atom is static due to the back bonds with three neighboring X atoms. Interestingly, the peak frequency of these vibration modes reveal lots of physical and chemical detail of the local environment of the excited dipole X-H vibration. Here we will shortly elaborate on this using the most extensive studied X-H vibration in literature, i.e. the silicon-hydrides in molecules, at surfaces of a-Si:H and c-Si:H, and in the bulk of a-Si:H, nc-Si:H and hydrogen implanted c-Si [78] as shown in Fig. 4**A**. The dielectric nature of a medium of vibrating dipoles can be described by the superposition of Lorentz-Lorenz dipole oscillators [10]:

$$10^{-4}\sum_j N_j \frac{q_{0,j}^2\Omega_j^2}{4\pi^2 c^2 m_j \epsilon_0}\left(\frac{1}{\omega^2-\omega_{0,j}^2+2i\delta_j\omega}\right)=3\frac{\epsilon(\omega)-1}{\epsilon(\omega)+2} \quad (1)$$

With $\epsilon(\omega)$ the dielectric function of the medium of vibrating dipoles. Every type of X-H vibration has it own eigenfrequency (ω_0) depending on the effective charge (q_0)(unscreened), effective dipole mass (m) and screening of its surrounding, as described by Ω. The X-H vibrations in a free molecule can be considered as 'unscreened' dipole vibrations and reside in molecules like silane (SiH_4) and polysilane (Si_nH_{2n+2}). The 'unscreened' frequency is determined by the hydride nature, i.e. mono-, di-, tri-, and tetra-hydrides as shown in Fig. 4**B**. From Eq. (1) it can be derived that subtle frequency shifts ($\Delta\omega$) in reference to the 'unscreened' eigenfrequency are given by:

$$\Delta\omega_j = -\frac{10^{-4}}{24\pi^2 c^2 m_j \omega_{0,j}\epsilon_0}\frac{K_j q_{0,j}^2\Omega_j^2}{V_{Si}} \quad (2)$$

where parameter K is the nano-structure parameter reflecting the averaged number of Si-H dipoles per volume unit V of one missing Si in the Si:H network [10,79]. It are these subtle frequency shifts that can reveal the physical nature of the dipole vibrations. First, the effect of electrical screening is illustrated in Fig. 4**A–B**. The eigenfrequency of 'unscreened' silicon hydrides shifts from larger frequencies in (poly-) silane molecules to lower frequencies when the hydride types are bonded to a surface. Here the dipole vibration experiences an electrical screening by the dielectric nature of the sub-surface solid. Screening means that the effective charge of the dipole is altered due the dielectric medium around it in reference to the unscreened dipole (ω_0 ~ 3020 cm^{-1}, ~ 2189 cm^{-1}, ~ 2110 cm^{-1} and ~ 1908 cm^{-1} for CH_4, SiH_4, GeH_4 and SnH_4). Maximum screening is obtained when the dipole vibration is incorporated in the bulk with locally a high dielectric constant. This is demonstrated by the Ge-based alloys in Fig. 5. In this figure, the frequency ranges are visualized of all carbon, silicon and germanium hydride and oxide vibrational modes observed in this work. Fig. 5 shows that Ge:H has the lowest wavenumber for the hydride wagging, bending and stretching modes, as well as oxide stretching modes, and the largest shifts $\Delta\omega$ in reference to the unscreened ω_0. The C-(O,H) SMs appear up-shifted in reference to Si-(O,H) SMs, which appear up-shifted in reference to Ge-(O,H), which is in line with the fact that Ge:H has the highest dielectric constant of all IV-valence alloys studied in this paper.

The typical tetrahedral coordination of IV-valence alloys basically defines the K-values of the various hydrogenated volume deficiencies. A monovacancy is in theory a vacancy in which 4 hydrogen atoms can be incorporated and replace one silicon atom (VH_4 where 'V' is the missing Si atom monohydride density of $K = 4$). The monohydride can be incorporated in polyvacancies as well. For these small polymer-like shaped vacancies the general relation is valid that in an m-vacancy, m silicons are replaced by 2 m+ 2 hydrogen atoms (V_mH_{2m+2}). For polyvacancies with m ≥ 3 the centered V positions accommodate two hydrogens instead of the three hydrogens as at the polyvacancy ends. For a divacancy, the local monohydride densities are represented by $K = 3$ and for a trivacancy by both $K = 3$ and $K = 2$ (H_3V-$(VH_2)_{m-2}$-VH_3). Experimental evidence exists that deficiencies with equivalent sizes to divacancies exist in a-Si:H. Nuclear magnetic resonance spectroscopy [80], small-angle neutron scattering [81], positron annihilation studies [82,83] as well as density analysis [11] have shown that hydrogen is predominantly clustered together with 6H atoms in dense a-Si:H. If the vacancy becomes larger than a polymer-chain of missing silicon atoms, we define the 'hole' in the matrix as a nanosized void. Small-angle X-ray scattering measurements on a-Si:H films deposited with several techniques show that mainly nanosized voids with a typical diameters of 2–4 nm are present in the a-Si:H network [81,84]. These observations are corroborated by positron lifetime measurements [85] and density measurements [11]. In view of the typical defect densities in a-Si:H (10^{15}–10^{17} cm^{-3}), the surface has to be considered as almost fully hydrogen passivated and several hundreds of hydrogen atoms must be bonded to such an internal void surface. Consequently, the void surface can be interpreted as a normal a-Si:H surface. On these surfaces, similar to hydrogen passivated c-Si and a-Si surfaces, monohyrides and dihydrides are present. All configurations discussed above, are based upon a network of tetrahedral silicon sites, which reside in rings of 6 sites. However, just like on a crystalline or amorphous surface, the Si atoms at the edge of a vacancy can form or reconstruct to dimer configurations, i.e. the silicon atoms reside in a ring of 5 atoms. A monovacancy ($X_{1.1}H_6$) and divacancy (H_3X-$X_{1.1}H_5$) with a dimer reconstruction are shown in Fig. 4**C**. We have to note here, that the volume in the lattice of the Si atoms in a 5-ring is ~ 20 % larger, since the 5-ring resides in a volume at which 6 silicon atoms can reside. Two silicon dimers share a quarter of their volume with the vacancy site, which makes the volume of this vacancy site 10 % larger relative to a vacancy site without a dimer. These configurations reflect the most compact way to incorporate Si-H bonds into a silicon matrix and are only obtained by either hydrogen implantation in c-Si or at the interface between a-Si:H tissue and crystalline silicon grains in the bulk of the densest nc-Si:H films.Fig. 4**C** shows on the horizontal axis all silicon-hydride SMs observed in a-Si:H, nc-Si:H and hydrogen implanted c-Si. All these frequencies can be plotted versus its parameter K (vertical axis) of its corresponding local silicon-hydride density in the hydrogenated volume deficiencies. Note, that the same effective charge of the Si-H dipole $q_0 = 0.40e$ has been used, and therefore Fig. 4**C** clearly demonstrates the validity of Eq.2 for the same type of silicon hydride. In addition, Fig. 4 demonstrates in general the power of the infrared analyses: the various SM's directly reveal the type and densities of hydrogenated volume deficiencies in the material. It scales with the macroscopic density of the bulk material, but also reveals specific hydrogen passivations at the interface of a-Si:H tissue and reconstructed surfaces of nano-crystalline grains.

5. Raman spectra of a/nc-$Si_{X\geq 0}Ge_{1-X}$ and their alloys with C, O and Sn

Raman analysis of the films is presented in Fig. 1 and an overview of the observed peaks, and their suspected origin, is presented in Table 3. A discussion of the amorphous and crystalline vibrational modes and the application of Raman analysis is presented first, before the Raman-active hydrides, oxides and carbides are considered.

5.1. Amorphous and crystalline C, Si and Ge

Crystalline bulk material exhibits a single vibrational Raman mode, while in amorphous bulk materials generally four distinct Raman vibrational modes are present; the transverse acoustic (TA), transverse optic (TA) longitudinal acoustic (LA) and longitudinal optic (LO) phonon modes. The Raman TO/LA peaks provide an important analytic tool for a range of thin film applications. These Raman modes are used to determine the stoichiometric nature of alloys such as a-SiGe:H [17,29,67]. The ratio between the TO/LA vibrational modes in reference to the

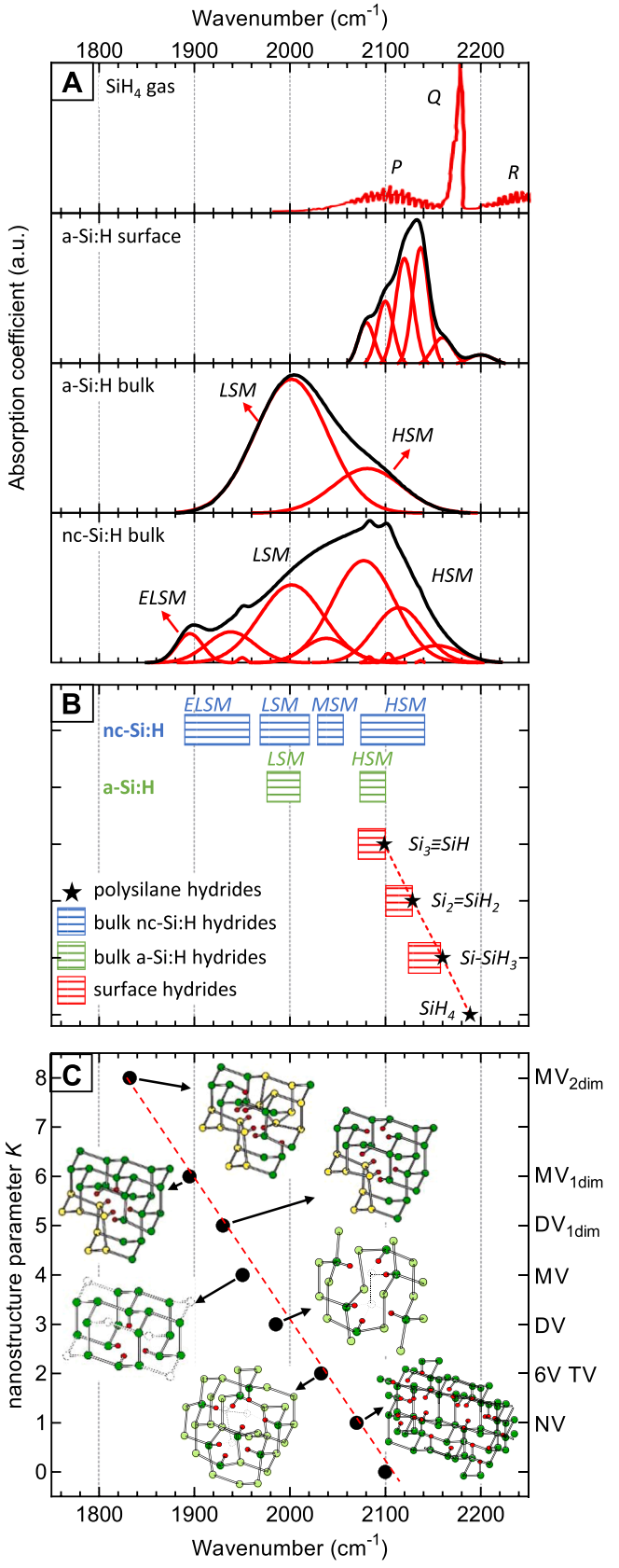

(caption on next column)

Fig. 4. **A)** Typical IR absorption spectra for SMs of hydrides in silane gas [76], on an a-Si:H surface and in the a-Si:H bulk and nc-Si:H bulk [52,77]. The absorption spectrum in the silane gas includes the typical P, Q and R-branches due to the rotational-vibrational coupled transitions of the molecule. The SM frequencies of the surface and bulk broaden and shift to lower values. **B)** The experimentally observed spectral ranges of Si-H SMs observed in (poly-)silane molecules, a-Si:H and nc-Si:H including the typical nomenclature adopted in this paper; extreme-low SM (ELSM), low SM (LSM), medium SM (MSM), high SM (HSM). Note that **B)** only has a horizontal axis, the vertical offset is applied for visualization purposes. Fig. **C)** all experimentally observed SMs in a-Si:H, nc-Si:H and hydrogen implanted c-Si versus the *K* parameter including the corresponding type of hydrogenated volume deficiency.

crystalline mode is used to determine the crystallinity in nc-Si:H [103, 104] and nc-Ge:H [26,71] films. Additionally, for nano-crystalline materials, in which nano-size crystals are embedded in an amorphous phase, the center peak frequency and width of the crystalline peak provides information used to determine the average size of silicon [37, 105] and germanium nanocrystals [89]. Moreover, for a crystalline alloy, the shift of the crystalline peak, in reference to an unalloyed crystal, can provide information about the stoichiometry of the crystalline phase, as demonstrated in experiments performed on SiGe [106] and GeSn crystals [24,107–109].

The four amorphous silicon modes are clearly visible in the a-Si:H and nc-Si:H samples. The a-Si:H TA and LA modes appear at 160 cm^{-1} and 320 cm^{-1}, as reported earlier [86]. As does the TO mode at 480 cm^{-1} [13,19,34,86]. The LO mode appears at about 440 cm^{-1}, which is unlike the traditionally reported 390 cm^{-1} [86] frequency but in line with more recent reports like [8,19]. Additionally, the peak related to the crystalline silicon phase, at 520 cm^{-1} is apparent in the nc-Si(O,C):H samples [19,96]. The Raman-active Ge vibrational modes are again shifted to lower wavenumbers with respect to their silicon counterparts. The amorphous germanium TA phonon mode at 80 cm^{-1} is positioned outside the range presented in this work. The LA mode at 177 cm^{-1}, LO mode at 230 cm^{-1} [34,87,88], and TO mode at 278 cm^{-1} [13,34,88,89] are clearly present in the measured a/nc-Ge:H spectra, in addition to the c-Ge peak at 300 cm^{-1} present in the spectrum of the nc-Ge:H film. [71,89–92]. The a-SiGe:H and nc-SiGe:H spectra are approximately a combination of the a/nc-Si:H and a/nc-Ge:H spectra. In these, a broad signal is apparent in the 100–550 cm^{-1} range, that is the superimposition of the various amorphous silicon and germanium modes. In addition to these modes, specific Si-Ge vibrational modes are present that appear in the 370–410 cm^{-1} range [13,86–88]. A visualization of the evolution of the different a-Si, a-Ge and a-SiGe Raman peaks as a function of the Ge-fraction in a large number of a-SiGe:H samples can be found elsewhere [29].

Additionally, an unexpected observation from the evolution of the Raman spectra over time, in Fig. 3, should be discussed. The intensity of the c-Si peak at 520 cm^{-1} in the nc-Si:H sample can be observed to increase over time. A similar intensification of the crystalline peak can be observed in the nc-Si(O):H sample and the nc-Ge:H sample, at 300 cm^{-1}. Although the cause of this post-deposition crystallization cannot be determined with any certainty, the most likely explanation is a thermally induced crystallization, resulting from conductivity measurements performed at 130 °C at 10–100–1000 h after deposition.

The behavior of carbon is dissimilar to that of its group-IV kin Si and Ge, in that carbon has the tendency to form double and triple covalent bonds involving 4–6 valence electrons. These so-called sp and sp2 hybridizations are unstable in Si and Ge, where exclusively sp3 hybridization occurs. This makes the exact interpretation of Raman spectra of amorphous carbon films more complex than their other group IV counterparts. Carbon-carbon bonds are generally present in the 1200–1650 cm^{-1} range [57,99]. More specifically, they appear as the diamond (D) bond with the peak frequency at ≈ 1320–1360 cm^{-1}, graphite (G) band with the peak frequency ≈ 1565–1590 cm^{-1} [45,51, 100–102] and two additional bands with peak frequencies at

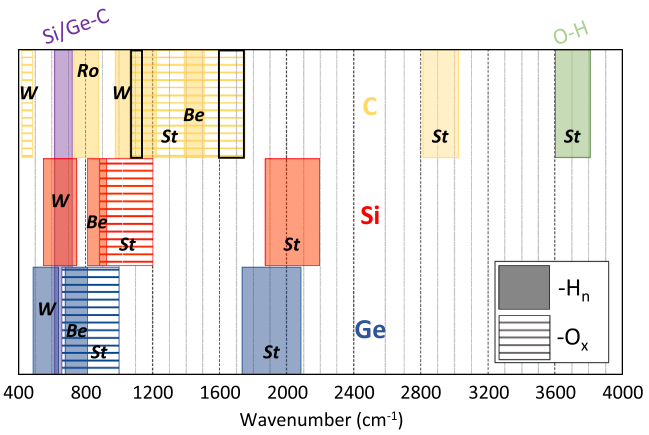

Fig. 5. Schematic representation of the vibrations observed in this work. Colored areas indicate width of observed vibrations, while black text indicates vibration type: rocking (*Ro*), wagging (*W*), bending (*Be*), stretching (*St*). Visual indicates O-H_n vibrations (top,green), C-(O_x,H_n) (top, yellow) vibrations, Si-(O_x, H_n) (center, red) and Ge-(O_x,H_n) vibrations (bottom, blue). Dashed area indicates range of O_x vibrations while even colored areas indicates range of H_n vibrations. Purple area indicates range of Si-C and Ge-C vibrations. Black squares present in yellow dashed range of C-O_x vibrations indicates specific C-O_x vibrations observed in this work.

Table 3
Raman peaks.

Peak frequency (cm^{-1})	Suspected vibration	Refs.
165–175	a-Si TA	[86]
170–180	a-Ge LA	[34,87,88]
230–250	a-Ge LO	[34,87,88]
270–280	a-Ge TO	[13,34,88,89]
300	c-Ge	[71,89–92]
320	a-Si LA	[86]
330	O-Ge-O/Ge-O-Ge	[93–95]
370–410	Si-Ge	[13,29,86–88]
430–440	a-Si LO	[8,19]
440	O-Ge-O/Ge-O-Ge	[93–95]
480	a-Si TO	[13,19,34,86]
520	c-Si	[19,96]
540–560[a]	Ge-H	
	O-Ge-O	[93–95]
	Ge-C	[57,70,75,97]
620–630	Si-H	[96]
800	Si-C TO	[98,99]
870–900	Si-H_n	
960	Si-O-Si	[19]
970	Si-C LO	[98,99]
1600	C-C (G-band)	[45,51,57,99–102]
1870–1890	Ge-H $_n$	
1900–2100	Si-H_n	
2800–3000	C-H_n	

[a] No definitive assignment can be made based on FTIR, Raman and EDX data.

≈ 1165–1190 cm^{-1} and ≈ 1485–1510 [99–101], where increased amorphization results in broadening of these bands. Of these bonds, only the G-band weakly appears in the a-GeC(Sn):H spectra at around 1600 cm^{-1}. The vibrations are accompanied by weak C-H_n vibrations in the 2800–3000 cm^{-1} range. Unlike the a-GeC:H spectrum, carbon-related vibrations do not seem to have a significant influence on the nc-SiC:H Raman spectrum. No features were apparent in the 1200–1650 a-C range or in the 2800–3000 C-H_n range. Also at ≈ 800 cm^{-1} and ≈ 970 cm^{-1}, where the Si-C TO and LO mode reportedly appear [98,99], the Raman spectra do not seem to differ significantly from the a/nc-Si:H and nc-SiO:H spectra.

5.2. Hydrides, oxides and carbides in Raman spectra

The FTIR active Si-H vibrational bonds are also Raman active, albeit not as strongly. The Si-H SMs appear more or less at the same frequency in the Raman spectrum. In both the a-Si:H and nc-Si:H spectra the Si-H wagging modes appear at 628 cm^{-1}, Si-H_n bending at 876–885 cm^{-1} and Si-H and Si-H_2 stretching in the 1900–2100 cm^{-1} range. Apart from these modes, the Ge-H SMs that appeared in FTIR spectra are also present in a/nc-Ge:H Raman spectra with peak frequencies at 540–560 cm^{-1} and 1880–1886 cm^{-1}. The peak at ≈ 960 cm^{-1} is likely related to Si-O-Si stretching [19]. This Si-O-Si peak is present in all silicon rich samples (a/nc-Si:H, nc-SiGe:H, nc-SiO:H, nc-SiC:H) presented in this work.

Three more wide, overlapping peaks are present in the a/nc-Ge:H Raman spectra that also appear in the a-GeO:H and a-GeC(Sn):H spectra, with peak frequencies at ≈ 340–350 cm^{-1}, ≈ 440 cm^{-1} and ≈ 540–560 cm^{-1}. While the latter is most likely the result of Ge-H wagging, it is challenging to determine the exact origin of former two peaks. Two of the peak frequencies roughly coincide with the amorphous silicon LA and LO modes. It cannot be excluded that during Ge:H plasma processing the heavy Ge-ion bombardment causes some amorphization of the silicon wafer, resulting a thin amorphous silicon layer. These silicon elements would not appear in the EDX measurements, since a low enough acceleration energy was used as to not probe the silicon surface. However, if they feature this strongly in the Raman spectra, Si-H_n or Si-Ge vibrations would be expected in the FTIR and Raman spectra, respectively, but such vibrations are absent. Considering the EDX measurements, Ge-O related vibrations are a more likely origin of the these peaks. Little information is available regarding Raman vibrations in amorphous GeO_x. Research into the Raman spectra of quartz-like GeO_x structures indicate that the twisting vibrations of O-Ge-O bonds and Ge-O-Ge bonds appear at 330, 440 and 530 cm^{-1} [93–95], which coincide well with the peak frequencies in this work. It should be noted that with respect to the quartz-like GeO_x structures, the peaks in this work are wider. This is in line with expectations, since in hydrogenated amorphous structures there is a much greater range of available back-bonded configurations. Another potential origin for the peak at ≈ 540 cm^{-1} in the a-GeC(Sn):H Raman spectrum are Ge-C vibrations [57,70,75,97]. The peaks at 1600 cm^{-1} and 2800–3000 cm^{-1} do in fact indicate the presence of small fractions of C-C and C-H_n bonds in the a-GeC:H sample.

6. Reflection on the fitting process of heterogeneous group IV alloys

Finally, a reflection on the fitting of vibrational spectra. As discussed in section 4. the peak frequency is determined by the local X-H dipole density of its corresponding incorporation configuration. The width of the peak is determined by the local distortion in reference to a tetrahedrally coordinated nature of most IV-valence materials. Here we distinguish three possibilities: an amorphous matrix, a crystalline lattice and the interface between amorphous and crystalline phase. The peak widths corresponding to X-H within a fully crystalline nature are narrow (< 5 cm^{-1} at full width at half maximum (FWHM)), like seen for the Si-H on hydrogenated crystalline grains, the so-called NHSMs. The X-H vibration modes in an amorphous local environment have the broadest width, for example the LSM and HSM for a-Si:H tissue (≈ 58 cm^{-1} at FWHM). In between are the hydrogenated volume deficiencies at the border of the amorphous and crystalline phase, reflected by example by the ELSM (≈ 24 cm^{-1} at FWHM). A consequence of this is that the widths of the peaks are limited to three typical widths corresponding to these three phases. This general guideline of three classes of peak widths is a helpful tool in the determination of the number of Gaussians to be chosen for fitting the spectrum with a physical relevant interpretation. Note, that two peaks for which the difference in their peak frequency is smaller than the width of the two peaks will not result a an unique fitting

solution. If this would correspond to a physical reality it would mean that both corresponding dipole vibrations cannot be uniquely resolved. However, even with these specific guidelines, the fitting of vibrational spectra can be subjective, especially with increasing film heterogeneity, so with increasing chemical and structural complexity. This is exemplified by three observations from this work.

1. For the nc-Si:H samples in Fig. 4**A** it is demonstrated, based on a large set of samples with a wide variety of Si:H phases, that a total of 11 Gaussians should be fitted to account for all potential Si-H stretching modes in the nc-Si:H bulk environment. In Fig. 1 a good fit was achieved for nc-Si:H with three Gaussian distributions and a decent fit could be achieved with only two Gaussians. Adding additional Gaussians to the fitting of the sample in Fig. 1 would be an arbitrary process, unless the exact number, center frequency and width of the Gaussians are known. This requires intricate prior knowledge of the material that is to be fitted, which is often not available.
2. Even if extensive prior knowledge is available, simplification during the fitting procedure might be required. In the nc-Si:H Raman spectrum in Fig. 1 for instance, six peaks are fitted in the < 530 cm^{-1} wavenumber region; four peaks for the various amorphous phonon modes, a single peak for the c-Si vibrational mode and an additional peak at 510 cm^{-1}. The 510 cm^{-1} peak accounts for the fact that the exact peak position of a silicon crystal, on a nanometer scale, is crystal-size dependent. A fit true to nature would therefore require a very large number of narrow Gaussians, each representing a particular crystal size. In Fig. 1 a single Gaussian is added to compensate for the effect of frequency shift as a function of crystal size, since a single Gaussian (in addition to regular amorphous and crystalline modes) could accurately represent the measured data. However, compensating for this effect in the fitting process is inherently subjective.
3. In Section 3.2 it was indicated that a large number of vibrations was reported in the 650–950 cm^{-1} range in a/nc-Ge(O,C):H films. This multitude of vibrational modes reported in this range is unsurprising. For these chemically complex alloys, the absorbance in this range is the result of the superimposition of a large number of vibrational modes resulting from different bonding configuration between Ge, C, O and H. This is evident considering, for instance, the vibrational spectra of a-GeO:H and a-GeC:H post deposition, in the insets in Fig. 3. In these insets the Gaussians widen and the center peak frequency shifts under influence of post-deposition oxidation. The reported peak frequency for Ge samples with traces of oxygen, carbon and hydrogen, will therefore not only be a function of the ratio of different bonds present in the material, but also of the assumptions during the fitting procedure regarding baseline subtraction and the number of vibrational modes.

The three examples demonstrate that the fitting of vibrational spectra of chemically and/or structurally complex films can be a subjective process, in which assumptions, prior knowledge and the level of detail of the metrics one tries to obtain from the fitting process plays a role. If, for instance, the purpose is to identify the local configurations of hydrogen incorporation, the spectra need to be fitted with a limited number of Gaussians which all have a physical relevant fixed peak width corresponding to one of the three phases. However, if the purpose is to identify the chemical composition of the bulk, the fitting approach using the lowest number of Gaussians for a unique fit will be sufficient.

7. Conclusion

In this work, the vibrational modes present in hydrogenated, oxygenated and carbonated group IV alloys are investigated. Raman and infrared spectroscopy measurements are performed in combination with elemental analysis to identify vibrational modes in a unique range of amorphous and nano-crystalline $Si_{X\geq 0}Ge_{1-X}$:H films and their alloys with C, O and Sn. Measurements are performed both post-deposition and following extended exposure to the ambient and DI water. This comprehensive review is of value as a reference for group IV peak identification. The effect of electrical screening, the influence of the dielectric medium on the peak frequency of a vibrational mode, is illustrated using the experimentally observed frequency shifts of bending, wagging and stretching vibrations of C-H in reference to Si-H, and Si-H in reference to Ge-H. Similar shifts are demonstrated for C-O stretching modes in reference to Si-O and Ge-O. Additionally, all experimentally observed frequencies of silicon hydride stretching modes in silicon solids and corresponding silicon-hydride configurations are identified using a straightforward Lorentz-Lorenz model approximation and considering all potential hydrogenated volume deficiencies within tetrahedrally coordinated amorphous and nanocrystalline lattice. It shows that the stretching mode signature can reveal detailed information on the volume deficiencies in IV-valence alloys.

Declaration of Competing Interest

The authors declare that they have no known competing financial interests or personal relationships that could have appeared to influence the work reported in this paper.

Acknowledgments

The authors would like to gratefully acknowledge the financial support from the Netherlands Organization for Scientific Research (NWO) Solar to Products grant awarded to Arno Smets and the support provided by Shell International Exploration & Production New Energies Research & Technology Dense Energy Carriers Program.

References

[1] M. Zacharias, J. Blasing, Preparation of a-GeO$_x$:H alloys: vibrational, optical, and structural properties, Phys. Rev. B 52 (19) (1995) 14018–14024, https://doi.org/10.1103/PhysRevB.52.14018.
[2] B.P. Nelson, Y. Xu, J.D. Webb, A. Mason, R.C. Reedy, L.M. Gedvilas, W. A. Lanford, Techniques for measuring the composition of hydrogenated amorphous silicon-germanium alloys, J. Non-Cryst. Solids 269 (2000) 680–684, https://doi.org/10.1016/S0022-3093(99)00848-0.
[3] M. Li, L. Jiang, Y. Sun, T. Xiao, P. Xiang, X. Tan, Silicon content influence on structure and photoluminescence properties of carbon rich hydrogenated amorphous silicon carbide thin films, J. Alloy. Compd. 753 (2018) 320–328, https://doi.org/10.1016/j.jallcom.2018.04.226.
[4] Y.H. Chen, H.Y. Fang, C.M. Yeh, Raman scattering and electrical characterizations studies of hydrogenated amorphous silicon-germanium alloys prepared by 40 MHz plasma-enhanced CVD, J. Non-Cryst. Solids 357 (1) (2011) 1–3, https://doi.org/10.1016/j.jnoncrysol.2010.09.060.
[5] D. Bermejo, M. Cardona, Infrared absorption in hydrogenated amorphous and crystallized germanium, J. Non-Cryst. Solids 32 (1–3) (1979) 421–430, https://doi.org/10.1016/0022-3093(79)90086-3.
[6] A.H.M. Smets, M.A. Wank, B. Vet, M. Fischer, R.A.C.M.M. van Swaaij, M. Zeman, D.C. Bobela, C.R. Wronski, M.C.M. van de Sanden, The relation between the band gap and the anisotropic nature of hydrogenated amorphous silicon, in: Proceedings of the 2011 37th IEEE Photovoltaic Specialists Conference, IEEE, 2011, 003342–003342. ⟨https://doi.org/10.1109/PVSC.2011.6186662⟩.
[7] K. Eberhardt, G. Bauer, Effect of H-content and H-bonding configuration on light and thermal induced metastability in amorphous hydrogenated germanium (a-Ge:H), J. Non-Cryst. Solids 164–166 (PART 1) (1993) 19–22, https://doi.org/10.1016/0022-3093(93)90482-D.
[8] V.A. Volodin, D.I. Koshelev, Quantitative analysis of hydrogen in amorphous silicon using Raman scattering spectroscopy, J. Raman Spectrosc. 44 (12) (2013) 1760–1764, https://doi.org/10.1002/jrs.4408.
[9] B. Najafov, V. Figarov, Hydrogen content evaluation in hydrogenated nanocrystalline silicon and its amorphous alloys with germanium and carbon, Int. J. Hydrog. Energy 35 (9) (2010) 4361–4367, https://doi.org/10.1016/j.ijhydene.2010.02.061.
[10] A.H.M. Smets, M.C.M. van de Sanden, Relation of the Si-H stretching frequency to the nanostructural Si-H bulk environment, Phys. Rev. B 76 (7) (2007), 073202, https://doi.org/10.1103/PhysRevB.76.073202.
[11] A.H.M. Smets, W.M.M. Kessels, M.C.M. van de Sanden, Vacancies and voids in hydrogenated amorphous silicon, Appl. Phys. Lett. 82 (10) (2003) 1547–1549, https://doi.org/10.1063/1.1559657.
[12] J. Melskens, A. Schnegg, A. Baldansuren, K. Lips, M.P. Plokker, S.W.H. Eijt, H. Schut, M. Fischer, M. Zeman, A.H.M. Smets, Structural and electrical

properties of metastable defects in hydrogenated amorphous silicon, Phys. Rev. B 91 (24) (2015), 245207, https://doi.org/10.1103/PhysRevB.91.245207.
[13] Y.-P. Chou, S.-C. Lee, Structural, optical, and electrical properties of hydrogenated amorphous silicon germanium alloys, J. Appl. Phys. 83 (8) (1998) 4111–4123, https://doi.org/10.1063/1.367229.
[14] M.A. Wank, R.A.C.M.M. van Swaaij, P. Kudlacek, M.C.M. van de Sanden, M. Zeman, Hydrogenated amorphous silicon deposited under accurately controlled ion bombardment using pulse-shaped substrate biasing, J. Appl. Phys. 108 (10) (2010), 103304, https://doi.org/10.1063/1.3505794.
[15] G. Lucovsky, S.S. Chao, J. Yang, J.E. Tyler, R.C. Ross, W. Czubatyj, Chemical bonding of hydrogen and oxygen in glow-discharge-deposited thin films of a-Ge:H and a-Ge:(H,O), Phys. Rev. B 31 (4) (1985) 2190–2197, https://doi.org/10.1103/PhysRevB.31.2190.
[16] B. Schröder, A. Annen, T. Drüsedau, H. Freistedt, P. Deák, H. Oechsner, Influence of oxygen incorporation on the properties of magnetron sputtered hydrogenated amorphous germanium films, Appl. Phys. Lett. 62 (16) (1993) 1961–1963, https://doi.org/10.1063/1.109504.
[17] A. Bhaduri, P. Chaudhuri, S. Vignoli, C. Longeaud, Correlation of structural inhomogeneities with transport properties in amorphous silicon germanium alloy thin films, Sol. Energy Mater. Sol. Cells 94 (9) (2010) 1492–1495, https://doi.org/10.1016/j.solmat.2010.02.043.
[18] M. Niwano, J. Kageyama, K. Kurita, K. Kinashi, I. Takahashi, N. Miyamoto, Infrared spectroscopy study of initial stages of oxidation of hydrogen-terminated Si surfaces stored in air, J. Appl. Phys. 76 (4) (1994) 2157–2163, https://doi.org/10.1063/1.357627.
[19] T. de Vrijer, A.H. Smets, The relation between precursor gas flows, thickness dependent material phases, and opto-electrical properties of doped a/nc-$SiO_{x\geq 0}$:H films, IEEE J. Photovolt. 11 (3) (2021) 591–599, https://doi.org/10.1109/JPHOTOV.2021.3059940.
[20] A. Bronneberg, A. Smets, M. Creatore, M. van de Sanden, On the oxidation mechanism of microcrystalline silicon thin films studied by Fourier transform infrared spectroscopy, J. Non-Cryst. Solids 357 (3) (2011) 884–887, https://doi.org/10.1016/j.jnoncrysol.2010.11.001.
[21] T. de Vrijer, J.E. van Dingen, P.J. Roelandschap, K. Roodenburg, A.H. Smets, Improved PECVD processed hydrogenated germanium films through temperature induced densification, Mater. Sci. Semicond. Process. 138 (2022), 106285, https://doi.org/10.1016/j.mssp.2021.106285.
[22] M. Katiyar, J.R. Abelson, Investigation of hydrogen induced phase transition from a-Si:H to μ c-Si:H using real time infrared spectroscopy, Mater. Sci. Eng.: A 304–306 (1–2) (2001) 349–352, https://doi.org/10.1016/S0921-5093(00)01528-8.
[23] M. Python, D. Dominé, T. Söderström, F. Meillaud, C. Ballif, Microcrystalline silicon solar cells: effect of substrate temperature on cracks and their role in post-oxidation, Prog. Photovolt.: Res. Appl. 18 (7) (2010) 491–499, https://doi.org/10.1002/pip.956.
[24] T. de Vrijer, K. Roodenburg, F. Saitta, T. Blackstone, G. Limodio, A.H. Smets, PECVD processing of low bandgap-energy amorphous hydrogenated germanium-tin (a-GeSn:H) films for opto-electronic applications, Appl. Mater. Today 27 (2022), 101450, https://doi.org/10.1016/j.apmt.2022.101450.
[25] M. Wojdyr, Fityk: a general-purpose peak fitting program, J. Appl. Crystallogr. 43 (5) (2010) 1126–1128, https://doi.org/10.1107/S0021889810030499.
[26] T. de Vrijer, A. Ravichandran, B. Bouazzata, A.H. Smets, The impact of processing conditions and post-deposition oxidation on the opto-electrical properties of hydrogenated amorphous and nano-crystalline Germanium films, J. Non-Cryst. Solids 553 (2021), 120507, https://doi.org/10.1016/j.jnoncrysol.2020.120507.
[27] T. de Vrijer, A.H.M. Smets, Infrared analysis of catalytic CO_2 reduction in hydrogenated germanium, Phys. Chem. Chem. Phys. (2022), https://doi.org/10.1039/D2CP01054B.
[28] T. de Vrijer, B. Bouazzata, A. Ravichandran, J. van Dingen, P. Roelandschap, K. Roodenburg, S. Roerink, F. Saitta, T. Blackstone, A. Smets, Opto-electrical properties of group IV alloys: the inherent challenges of processing hydrogenated germanium, Adv. Sci. (2022), https://doi.org/10.1002/advs.202200814.
[29] T. de Vrijer, H. Parasramka, S.J. Roerink, A.H. Smets, An expedient semi-empirical modelling approach for optimal bandgap profiling of stoichiometric absorbers: a case study of thin film amorphous silicon germanium for use in multijunction photovoltaic devices, Sol. Energy Mater. Sol. Cells 225 (2021), 111051, https://doi.org/10.1016/j.solmat.2021.111051.
[30] I. Omkaram, R. SreekanthChakradhar, J. LakshmanaRao, EPR, optical, infrared and Raman studies of VO^{2+} ions in polyvinylalcohol films, Phys. B: Condens. Matter 388 (1–2) (2007) 318–325, https://doi.org/10.1016/j.physb.2006.06.134.
[31] E. Abdelrazek, A. Abdelghany, A. Tarabiah, Characterization and physical properties of silver/PVA nano-composite, Res. J. Pharmaceut. Biol. Chem. Sci. 3 (4) (2012) 448–459.
[32] W. Paul, Structural, optical and photoelectronic properties of improved PECVD a-Ge:H, J. Non-Cryst. Solids 137–138 (1991) 803–808, https://doi.org/10.1016/S0022-3093(05)80242-X.
[33] I. Chambouleyron, F.C. Marques, J.P. de Souza, I.J.R. Baumvol, Structure and composition of amorphous $Ge_{1-x}Sn_x$ thin films, J. Appl. Phys. 63 (11) (1988) 5596–5598, https://doi.org/10.1063/1.340338.
[34] O. Madelung, M. Schulz, H. Weiss, Numerical Data and Functional Relationships in Science and Technology: Special Systems and Topics. Comprehensive Index for III/17, Springer-Verlag, Berlin, Heidelberg, New York, Toky, 1985.
[35] A. Fedala, R. Cherfi, M. Aoucher, T. Mohammed-Brahim, Structural, optical and electrical properties of hydrogenated amorphous silicon germanium (a-$Si_{1-x}Ge_x$) deposited by DC magnetron sputtering at high rate, Mater. Sci. Semicond. Process. 9 (4–5) (2006) 690–693, https://doi.org/10.1016/j.mssp.2006.08.016.
[36] M. Cardona, Vibrational spectra of hydrogen in silicon and germanium, Phys. Status Solidi (b) 118 (2) (1983) 463–481, https://doi.org/10.1002/pssb.2221180202.
[37] M. Künle, T. Kaltenbach, P. Löper, A. Hartel, S. Janz, O. Eibl, K.-G. Nickel, Si-rich a-SiC:H thin films: structural and optical transformations during thermal annealing, Thin Solid Films 519 (1) (2010) 151–157, https://doi.org/10.1016/j.tsf.2010.07.085.
[38] M. Gazicki, Plasma deposition of thin carbon/germanium alloy films from organogermanium compounds, Chaos Solitons Fractals 10 (12) (1999) 1983–2017, https://doi.org/10.1016/S0960-0779(98)00246-X.
[39] W. Sah, H. Tsai, S. Lee, Physical and electronic structure of amorphous silicon carbon hydrogen alloy, Appl. Phys. Lett. 54 (7) (1989) 617–619, https://doi.org/10.1063/1.100896.
[40] S. Ray, D. Das, A. Barua, Infrared vibrational spectra of hydrogenated amorphous silicon carbide thin films prepared by glow discharge, Sol. Energy Mater. 15 (1987) 45–57, https://doi.org/10.1016/0165-1633(87)90075-X.
[41] A. Lukianov, N. Klyui, B. Sha, M. Dusheiko, V. Lozinskii, A. Liptuga, V. Kasatkin, B. Liu, Nonstoichiometric amorphous silicon carbide films as promising antireflection and protective coatings for germanium in IR spectral range, Opt. Mater. 88 (2019) 445–450, https://doi.org/10.1016/j.optmat.2018.12.012.
[42] A. Kozak, O. Porada, V. Ivashchenko, L. Ivashchenko, P. Scrynskyy, T. Tomila, V. Manzhara, Comparative investigation of Si-C-N Films prepared by plasma enhanced chemical vapour deposition and magnetron sputtering, Appl. Surf. Sci. 425 (2017) 646–653, https://doi.org/10.1016/j.apsusc.2017.06.332.
[43] J. Xu, L. Yang, Y. Rui, J. Mei, X. Zhang, W. Li, Z. Ma, L. Xu, X. Huang, K. Chen, Photoluminescence characteristics from amorphous SiC thin films with various structures deposited at low temperature, Solid State Commun. 133 (9) (2005) 565–568, https://doi.org/10.1016/j.ssc.2004.12.036.
[44] Y. Catherine, G. Turban, Infrared absorption of hydrogenated amorphous Si-C and Ge-C films, Thin Solid Films 70 (1) (1980) 101–104, https://doi.org/10.1016/0040-6090(80)90416-2.
[45] C. Zoita, C. Grigorescu, I. Vasiliu, I. Feraru, Influence of process parameters on structure and optical properties of GeC thin films deposited by RF magnetron sputtering, Thin Solid Films 519 (12) (2011) 4101–4104, https://doi.org/10.1016/j.tsf.2011.01.204.
[46] I. Vivaldo, M. Moreno, A. Torres, R. Ambrosio, P. Rosales, N. Carlos, W. Calleja, K. Monfil, A. Benítez, A comparative study of amorphous silicon carbide and silicon rich oxide for light emission applications, J. Lumin. 190 (2017) 215–220, https://doi.org/10.1016/j.jlumin.2017.05.048.
[47] D. Bermejo, M. Cardona, Raman scattering in pure and hydrogenated amorphous, J. Non-Cryst. Solids 32 (1978) 405–419, https://doi.org/10.1016/0022-3093(79)90085-1.
[48] J. Szmidt, Electrophysical properties of thin germanium/carbon layers produced on silicon using organometallic radio frequency plasma enhanced chemical vapor deposition process, Thin Solid Films 441 (1–2) (2003) 192–199, https://doi.org/10.1016/S0040-6090(03)00884-8.
[49] J. Tyczkowski, P. Kazimierski, H. Szymanowski, Correlations between process parameters, chemical structure and electronic properties of amorphous hydrogenated Ge_xC_{1-x} films prepared by plasma-enhanced chemical vapour deposition in a three-electrode reactor, Thin Solid Films 241 (1–2) (1994) 291–294, https://doi.org/10.1016/0040-6090(94)90444-8.
[50] R. Cross, F. Glockling, Infrared spectra of organogermanes, J. Organomet. Chem. 3 (2) (1965) 146–155, https://doi.org/10.1016/S0022-328X(00)84744-0.
[51] N. Saito, I. Nakaaki, T. Yamaguchi, S. Yoshioka, S. Nakamura, Influence of deposition conditions on the properties of a-GeC:H and a-Ge:H films prepared by r.f. magnetron sputtering, Thin Solid Films 269 (1–2) (1995) 69–74, https://doi.org/10.1016/0040-6090(95)06671-3.
[52] A.H.M. Smets, T. Matsui, M. Kondo, High-rate deposition of microcrystalline silicon p-i-n solar cells in the high pressure depletion regime, J. Appl. Phys. 104 (3) (2008), 034508, https://doi.org/10.1063/1.2961334.
[53] G. Talukder, J.C.L. Cornish, P. Jennings, G.T. Hefter, B.W. Clare, J. Livingstone, Effects of annealing on infrared and thermal-effusion spectra of sputtered a-Si:H alloys, J. Appl. Phys. 71 (1) (1992) 403–409, https://doi.org/10.1063/1.350723.
[54] E. Abdelrazek, I. Elashmawi, A. El-khodary, A. Yassin, Structural, optical, thermal and electrical studies on PVA/PVP blends filled with lithium bromide, Curr. Appl. Phys. 10 (2) (2010) 607–613, https://doi.org/10.1016/j.cap.2009.08.005.
[55] A. Tawansi, A. Oraby, H. Zidan, M. Dorgham, Effect of one-dimensional phenomena on electrical, magnetic and ESR properties of $MnCl_2$-filled PVA films, Phys. B: Condens. Matter 254 (1–2) (1998) 126–133, https://doi.org/10.1016/S0921-4526(98)00414-1.
[56] M. Martin, Characteristic IR Band Positions.
[57] H. Jamali, R. Mozafarinia, A. Eshaghi, Evaluation of chemical and structural properties of germanium-carbon coatings deposited by plasma enhanced chemical vapor deposition, J. Alloy. Compd. 646 (2015) 360–367, https://doi.org/10.1016/j.jallcom.2015.06.091.
[58] N. Ojha, A. Bajpai, S. Kumar, Enriched oxygen vacancies of $Cu_2O/SnS_2/SnO_2$ heterostructure for enhanced photocatalytic reduction of CO_2 by water and nitrogen fixation, J. Colloid Interface Sci. 585 (2021) 764–777, https://doi.org/10.1016/j.jcis.2020.10.056.
[59] H. Zhang, Y. Li, J. Wang, N. Wu, H. Sheng, C. Chen, J. Zhao, An unprecedent hydride transfer pathway for selective photocatalytic reduction of CO_2 to formic acid on TiO_2, Appl. Catal. B: Environ. 284 (2021), 119692, https://doi.org/10.1016/j.apcatb.2020.119692.

[60] S.W. Pyo, C. Manianglung, Y.S. Ko, In-situ IR study on stability of amine-impregnated CO_2 adsorbents to acidic gases, Catal. Today 352 (2020) 198–203, https://doi.org/10.1016/j.cattod.2020.01.036.

[61] L. Wang, H. Tan, L. Zhang, B. Cheng, J. Yu, In-situ growth of few-layer graphene on ZnO with intimate interfacial contact for enhanced photocatalytic CO_2 reduction activity, Chem. Eng. J. 411 (2021), 128501, https://doi.org/10.1016/j.cej.2021.128501.

[62] C. Pirim, L. Krim, A neon-matrix isolation study of the reaction of non-energetic H-atoms with CO molecules at 3 K, Phys. Chem. Chem. Phys. 13 (43) (2011) 19454, https://doi.org/10.1039/c1cp21835b.

[63] Y. Yashiki, S. Kouketsu, S. Miyajima, A. Yamada, M. Konagai, Growth and characterization of germanium carbon thin films deposited by VHF plasma CVD technique, in: Proceedings of the 2006 IEEE 4th World Conference on Photovoltaic Energy Conference, 2, IEEE, 2006, pp. 1608–11. ⟨https://doi.org/10.1109/WCPEC.2006.279794⟩.

[64] T. Matsumoto, Y. Murata, J. Watanabe, Study of silicon-hydrogen bonds at an amorphous silicon/silicon nitride interface using infrared attenuated total reflection spectroscopy, Appl. Phys. Lett. 60 (16) (1992) 1942–1944, https://doi.org/10.1063/1.107158.

[65] D. Deligiannis, R. Vasudevan, A.H.M. Smets, R.A.C.M.M. van Swaaij, M. Zeman, Surface passivation of c-Si for silicon heterojunction solar cells using high-pressure hydrogen diluted plasmas, AIP Adv. 5 (9) (2015), 097165, https://doi.org/10.1063/1.4931821.

[66] W. Paul, D. Paul, B. vonRoedern, J. Blake, S. Oguz, Preferential attachment of H in amorphous hydrogenated binary semiconductors and consequent inferior reduction of pseudogap state density, Phys. Rev. Lett. 46 (15) (1981) 1016–1020, https://doi.org/10.1103/PhysRevLett.46.1016.

[67] L. Veldhuizen, C. van der Werf, Y. Kuang, N. Bakker, S. Yun, R. Schropp, Optimization of hydrogenated amorphous silicon germanium thin films and solar cells deposited by hot wire chemical vapor deposition, Thin Solid Films 595 (2015) 226–230, https://doi.org/10.1016/j.tsf.2015.05.055.

[68] Y. Toyoshima, K. Arai, A. Matsuda, K. Tanaka, In situ characterization of the growing a-Si:H surface by IR spectroscopy, J. Non-Cryst. Solids 137–138 (PART 2) (1991) 765–770, https://doi.org/10.1016/S0022-3093(05)80233-9.

[69] T. Matsui, M. Kondo, High-efficiency microcrystalline silicon and microcrystalline silicon-germanium alloy solar cells, MRS Proc. 1321 (5) (2011) 11–1321, https://doi.org/10.1557/opl.2011.1149.

[70] J. Zhu, C. Jiang, J. Han, H. Yu, J. Wang, Z. Jia, R. Chen, Optical and electrical properties of nonstoichiometric a-$Ge_{1-x}C_x$ films prepared by magnetron co-sputtering, Appl. Surf. Sci. 258 (8) (2012) 3877–3881, https://doi.org/10.1016/j.apsusc.2011.12.051.

[71] P. Klement, C. Feser, B. Hanke, K.V. Maydell, C. Agert, Correlation between optical emission spectroscopy of hydrogen/germane plasma and the Raman crystallinity factor of germanium layers, Appl. Phys. Lett. 102 (15) (2013), 152109, https://doi.org/10.1063/1.4802028.

[72] J. Coates, Interpretation of infrared spectra, a practical approach. Encyclopedia of Analytical Chemistry, 2004, pp. 1–23.

[73] A.B.D. Nandiyanto, R. Oktiani, R. Ragadhita, How to read and interpret ftir spectroscope of organic material, Indones. J. Sci. Technol. 4 (1) (2019) 97–118, https://doi.org/10.17509/ijost.v4i1.15806.

[74] C. Hu, L. Qiao, H. Tian, X. Lu, Q. Jiang, W. Zheng, Role of carbon in the formation of hard $Ge_{1-x}C_x$ thin films by reactive magnetron sputtering, Phys. B: Condens. Matter 406 (13) (2011) 2658–2662, https://doi.org/10.1016/j.physb.2011.01.077.

[75] C. Jiang, J. Zhu, J. Han, Z. Jia, X. Yin, Chemical bonding and optical properties of germanium-carbon alloy films prepared by magnetron co-sputtering as a function of substrate temperature, J. Non-Cryst. Solids 357 (24) (2011) 3952–3956, https://doi.org/10.1016/j.jnoncrysol.2011.08.014.

[76] P.W. Morrison, J.R. Haigis, In situ infrared measurements of film and gas properties during the plasma deposition of amorphous hydrogenated silicon, J. Vac. Sci. Technol. A: Vac. Surf. Films 11 (3) (1993) 490–502, https://doi.org/10.1116/1.578761.

[77] A.H.M. Smets, T. Matsui, M. Kondo, Infrared analysis of the bulk silicon-hydrogen bonds as an optimization tool for high-rate deposition of microcrystalline silicon solar cells, Appl. Phys. Lett. 92 (3) (2008), 033506, https://doi.org/10.1063/1.2837536.

[78] H.J. Stein, S.M. Myers, D.M. Follstaedt, Infrared spectroscopy of chemically bonded hydrogen at voids and defects in silicon, J. Appl. Phys. 73 (6) (1993) 2755–2764, https://doi.org/10.1063/1.353050.

[79] M. Fischer, H. Tan, J. Melskens, R. Vasudevan, M. Zeman, A.H.M. Smets, High pressure processing of hydrogenated amorphous silicon solar cells: relation between nanostructure and high open-circuit voltage, Appl. Phys. Lett. 106 (4) (2015), 043905, https://doi.org/10.1063/1.4907316.

[80] J. Baum, K.K. Gleason, A. Pines, A.N. Garroway, J.A. Reimer, Multiple-quantum NMR study of clustering in hydrogenated amorphous silicon, Phys. Rev. Lett. 56 (13) (1986) 1377–1380, https://doi.org/10.1103/PhysRevLett.56.1377.

[81] E. Gericke, J. Melskens, R. Wendt, M. Wollgarten, A. Hoell, K. Lips, Quantification of nanoscale density fluctuations in hydrogenated amorphous silicon, Phys. Rev. Lett. 125 (18) (2020), 185501, https://doi.org/10.1103/PhysRevLett.125.185501.

[82] J. Melskens, A.H.M. Smets, M. Schouten, S.W.H. Eijt, H. Schut, M. Zeman, New insights in the nanostructure and defect states of hydrogenated amorphous silicon obtained by annealing, IEEE J. Photovolt. 3 (1) (2013) 65–71, https://doi.org/10.1109/JPHOTOV.2012.2226870.

[83] J. Melskens, A. Smets, S. Eijt, H. Schut, E. Brück, M. Zeman, The nanostructural analysis of hydrogenated silicon films based on positron annihilation studies, J. Non-Cryst. Solids 358 (17) (2012) 2015–2018, https://doi.org/10.1016/j.jnoncrysol.2012.01.037.

[84] A.H. Mahan, Y. Xu, D.L. Williamson, W. Beyer, J.D. Perkins, M. Vanecek, L. M. Gedvilas, B.P. Nelson, Structural properties of hot wire a-Si:H films deposited at rates in excess of 100 Å/s, J. Appl. Phys. 90 (10) (2001) 5038–5047, https://doi.org/10.1063/1.1407317.

[85] V.G. Bhide, R.O. Dusane, S.V. Rajarshi, A.D. Shaligram, S.K. David, Positron-lifetime studies of hydrogenated amorphous silicon, J. Appl. Phys. 62 (1) (1987) 108–116, https://doi.org/10.1063/1.339167.

[86] H. Fritzsche, Amorphous Silicon and Related Materials, World Scientific Publishing Co. Pte. Ltd, Singapore, 1989.

[87] D. Bermejo, M. Cardona, Raman scattering in pure and hydrogenated amorphous germanium and silicon, J. Non-Cryst. Solids 32 (1–3) (1979) 405–419, https://doi.org/10.1016/0022-3093(79)90085-1.

[88] O. Madelung, U. Rossler, M. Schulz, Germanium (Ge) Raman phonon frequencies and wavenumbers, in: Group IV Elements, IV–IV and III–V Compounds. Part A – Lattice Properties, 4, Springer-Verlag, Berlin/Heidelberg, 2001, pp. 1–17, https://doi.org/10.1007/10551045_228.

[89] V.A. Volodin, G.K. Krivyakin, G.D. Ivlev, S.L. Prokopyev, S.V. Gusakova, A. A. Popov, Crystallization of amorphous germanium films and multilayer a-Ge/a-Si structures upon exposure to nanosecond laser radiation, Semiconductors 53 (3) (2019) 400–405, https://doi.org/10.1134/S1063782619030217.

[90] Y. Maeda, Visible photoluminescence from nanocrystallite Ge embedded in a glassy SiO_2 matrix: evidence in support of the quantum-confinement mechanism, Phys. Rev. B 51 (3) (1995) 1658–1670, https://doi.org/10.1103/PhysRevB.51.1658.

[91] V.A. Volodin, D.V. Marin, V.A. Sachkov, E.B. Gorokhov, H. Rinnert, M. Vergnat, Applying an improved phonon confinement model to the analysis of Raman spectra of germanium nanocrystals, J. Exp. Theor. Phys. 118 (1) (2014) 65–71, https://doi.org/10.1134/S1063776114010208.

[92] P. Alfaro-Calderón, M. Cruz-Irisson, C. Wang-Chen, Theory of Raman scattering by phonons in germanium nanostructures, Nanoscale Res. Lett. 3 (2) (2008) 55–59, https://doi.org/10.1007/s11671-007-9114-0.

[93] A. Zanatta, Temperature-dependent Raman scattering of the Ge + GeO_x system and its potential as an optical thermometer, Results Phys. 19 (2020), 103500, https://doi.org/10.1016/j.rinp.2020.103500.

[94] G. Fraysse, A. Lignie, P. Hermet, P. Armand, D. Bourgogne, J. Haines, B. Ménaert, P. Papet, Vibrational origin of the thermal stability in the highly distorted α-quartz-type material GeO_2: an experimental and theoretical study, Inorg. Chem. 52 (12) (2013) 7271–7279, https://doi.org/10.1021/ic4009416.

[95] J. Scott, Raman spectra of GeO_2, Phys. Rev. B 1 (8) (1970) 3488–3493, https://doi.org/10.1103/PhysRevB.1.3488.

[96] Z.P. Wang, H.X. Han, X.S. Zhao, G.H. Li, Si—Cl bonds in A-Si:H:Cl films, Solid State Commun. 58 (10) (1986) 709–711, https://doi.org/10.1016/0038-1098(86)90507-7.

[97] S.Y. Park, J. D'Arcy-Gall, D. Gall, Y.-W. Kim, P. Desjardins, J.E. Greene, C lattice site distributions in metastable $Ge_{1-y}C_y$ alloys grown on Ge(001) by molecular-beam epitaxy, J. Appl. Phys. 91 (6) (2002) 3644–3652, https://doi.org/10.1063/1.1448677.

[98] M. Losurdo, M. Giangregorio, P. Capezzuto, G. Bruno, F. Giorgis, Structural and optical investigation of plasma deposited silicon carbon alloys: Insights on Si—C bond configuration using spectroscopic ellipsometry, J. Appl. Phys. 97 (10) (2005), 103504, https://doi.org/10.1063/1.1899758.

[99] C. Srisang, P. Asanithi, K. Siangchaew, A. Pokaipisit, P. Limsuwan, Characterization of SiC in DLC/a-Si films prepared by pulsed filtered cathodic arc using Raman spectroscopy and XPS, Appl. Surf. Sci. 258 (15) (2012) 5605–5609, https://doi.org/10.1016/j.apsusc.2012.02.036.

[100] N. Gupta, B.P. Veettill, G. Conibeer, S. Shrestha, Effect of substrate temperature and radio frequency power on compositional, structural and optical properties of amorphous germanium carbide films deposited using sputtering, J. Non-Cryst. Solids 443 (2016) 97–102, https://doi.org/10.1016/j.jnoncrysol.2016.04.018.

[101] J. Hong, A. Goullet, G. Turban, Ellipsometry and Raman study on hydrogenated amorphous carbon (a-C:H) films deposited in a dual ECR-r.f. plasma, Thin Solid Films 352 (1–2) (1999) 41–48, https://doi.org/10.1016/S0040-6090(99)00298-9.

[102] J. Schwan, S. Ulrich, V. Batori, H. Ehrhardt, S.R.P. Silva, Raman spectroscopy on amorphous carbon films, J. Appl. Phys. 80 (1) (1996) 440–447, https://doi.org/10.1063/1.362745.

[103] C. Smit, R.A.C.M.M. van Swaaij, H. Donker, A.M.H.N. Petit, W.M.M. Kessels, M.C. M. van de Sanden, Determining the material structure of microcrystalline silicon from Raman spectra, J. Appl. Phys. 94 (5) (2003) 3582–3588, https://doi.org/10.1063/1.1596364.

[104] T. de Vrijer, F.T. Si, H. Tan, A.H.M. Smets, Chemical stability and performance of doped silicon oxide layers for use in thin-film silicon solar cells, IEEE J. Photovolt. 9 (1) (2019) 3–11, https://doi.org/10.1109/JPHOTOV.2018.2882650.

[105] L. Han, M. Zeman, A.H.M. Smets, Raman study of laser-induced heating effects in free-standing silicon nanocrystals, Nanoscale 7 (18) (2015) 8389–8397, https://doi.org/10.1039/C5NR00468C.

[106] D. Rouchon, M. Mermoux, F. Bertin, J. Hartmann, Germanium content and strain in $Si_{1-x}Ge_x$ alloys characterized by Raman spectroscopy, J. Cryst. Growth 392 (2014) 66–73, https://doi.org/10.1016/j.jcrysgro.2014.01.019.

[107] P. Pearcef, T. Wilsonf, A. Johnson, N. Ekins-Daukes, Characterization of SiGeSn for use as a 1 eV sub-cell in multi-junction solar cells, in: Proceedings of the 2018 IEEE 7th World Conference on Photovoltaic Energy Conversion (WCPEC) (A Joint

Conference of 45th IEEE PVSC, 28th PVSEC & 34th EU PVSEC), IEEE, 2018, pp. 0943–48. ⟨https://doi.org/10.1109/PVSC.2018.8547764⟩.

[108] N. vondenDriesch, D. Stange, S. Wirths, G. Mussler, B. Holländer, Z. Ikonic, J. M. Hartmann, T. Stoica, S. Mantl, D. Grützmacher, D. Buca, Direct bandgap group IV epitaxy on Si for laser applications, Chem. Mater. 27 (13) (2015) 4693–4702, https://doi.org/10.1021/acs.chemmater.5b01327.

[109] S. Su, W. Wang, B. Cheng, W. Hu, G. Zhang, C. Xue, Y. Zuo, Q. Wang, The contributions of composition and strain to the phonon shift in alloys, Solid State Commun. 151 (8) (2011) 647–650, https://doi.org/10.1016/j.ssc.2011.01.017.